Supplementary Material for

Interferometry with Bose-Einstein Condensates in Microgravity

H. Müntinga, H. Ahlers, M. Krutzik, A. Wenzlawski, S. Arnold, D. Becker,
K. Bongs, H. Dittus, H. Duncker, N. Gaaloul, C. Gherasim, E. Giese,
C. Grzeschik, T. W. Hänsch, O. Hellmig, W. Herr, S. Herrmann, E. Kajari,
S. Kleinert, C. Lämmerzahl, W. Lewoczko-Adamczyk, J. Malcolm, N. Meyer,
R. Nolte, A. Peters, M. Popp, J. Reichel, A. Roura, J. Rudolph,
M. Schiemangk, M. Schneider, S. T. Seidel, K. Sengstock, V. Tamma,
T. Valenzuela, A. Vogel, R. Walser, T. Wendrich, P. Windpassinger, W. Zeller,
T.van Zoest, W. Ertmer, W. P. Schleich, E. M. Rasel[*]

[*]To whom correspondence should be addressed; E-mail: rasel@iqo.uni-hannover.de

Materials and methods

In this supplementary material, more details about key experimental steps and the theoretical description are given. In the experimental part we provide details on the drop tower, the generation of the light grating for splitting and recombining the atomic ensembles, the state preparation & detection and the quantitative analysis of the absorption images of fringe patterns.

The theoretical description of the experimental results starts with a section briefly reviewing the scaling approach as a tool for describing the expansion dynamics of a Bose-Einstein condensate (BEC) for a time-dependent trapping potential. This is then applied to the asymmetric Mach-Zehnder interferometer (AMZI) of our experiment and all the relevant features of

the interference fringes at the exit ports are discussed. The complementarity of the interference patterns of the two exit ports as well as the case of the detection of overlapping ports are discussed in two separate sections.

Drop tower

Our free-fall experiments are carried out in the drop tower of the Center of Applied Space Technology and Microgravity in Bremen, Germany. Inside the 146 m tall tower, a 122 m high steel tube 3.5 m in diameter can be evacuated to around 10 Pa within 90 minutes. After a free fall of 4.7 s with residual accelerations in the parts per million range of the local gravity g, the sealed experimental capsule is caught in a 8 m high pool of polysterene balls. During the impact, the experiment has to sustain a deceleration of up to 50 g. A catapult mechanism housed beneath the tower allows us to launch a capsule upwards and thus double the free-fall time, which we plan to use in future experiments.

Light-induced Bragg scattering

Two light fields employed for Bragg scattering are generated by a single distributed feedback laser diode, which is stabilized with a detuning of 800 MHz to the $F = 2 \rightarrow F' = 3$ transition in the D$_2$-line of ^{87}Rb. The two beams pass an acousto-optic modulator (AOM) to generate the required relative offset frequency of 15 kHz. This technique provides us with precise control of the timing and the shape of the pulses. The light is then coupled into two polarization-maintaining fibers and guided to the vacuum chamber, where the two counterpropagating collimated beams of parallel linear polarization and diameter of 0.65 cm (FWHM) are formed. They are aligned parallel to the chip surface and perpendicular to the detection axis so that the interference fringes can be detected by means of absorption imaging. In the data presented, we use box-shaped pulses and Gaussian-shaped pulses. The experiments showed that the pulse shape

2

does not influence the contrast nor the signal of the interference pattern in the presented data. For this reason, we did not distinguish between the pulse shapes in Fig. 3.

State preparation

For the preparation of the BEC in the non-magnetic state $|F = 2, m_F = 0\rangle$ we an adiabatic rapid passage[35] (ARP). For the state transfer we apply a homogeneous static magnetic field of 11 G in x-direction and combine this with a 3.8 ms long RF-sweep from 7.714 MHz to 7.754 MHz. After the interferometer sequence a quadrupole field in Stern-Gerlach configuration is applied to split the atoms according to their hyperfine-state and to ensure that only atoms in the non-magnetic state contribute to the interference pattern. In this way we are also able to verify transfer efficiencies to the non-magnetic state of about 90%.

Detection and analysis of absorption images

The atomic clouds are probed with a laser beam on the $F = 2 \rightarrow F' = 3$ transition where the intensity of the detection beam is typically about 5% of the saturation intensity of the transition. Two images are taken in each experiment with a charge-coupled-device (CCD) camera (Hamamatsu C8484-15G): First the shadow of the cloud in the detection beam is recorded providing us with the intensity I_{atoms}. This beam heats the atoms and expels them from the imaging region. Then the detection beam is imaged in the absence of any atoms yielding I_{beam}. Both intensities I_{atoms} and I_{beam} are corrected for the camera dark image I_{dark} and we obtain the optical density

$$D \equiv \ln \left(\frac{I_{beam} - I_{dark}}{I_{atoms} - I_{dark}} \right), \tag{1}$$

and the atomic column density

$$n \equiv \frac{D}{\sigma} \tag{2}$$

with the resonant cross section σ.

3

To extract the contrast and the fringe spacing from the images of the interferometer output ports, we sum the column densities along z and fit the function

$$
\begin{aligned}
n_{1D} \equiv\; & n_{max,1D} \left[1 + C \sin \left(\frac{2\pi}{l}(y - y_1) + \varphi \right) \right] \exp \left(-\frac{(y - y_1)^2}{2\sigma_y^2} \right) \\
& + n_{max,1D} \left[1 + C \sin \left(\frac{2\pi}{l}(y - y_2) + \varphi + \pi \right) \right] \exp \left(-\frac{(y - y_2)^2}{2\sigma_y^2} \right) + n_{0,1D} \quad (3)
\end{aligned}
$$

to the 1D profiles with a nonlinear least squares method. Here, y_1 and y_2 are the centers of the two output ports, σ_y the width of their Gaussian envelopes, l the fringe spacing and C the contrast shown in Fig.3(a) and Fig.3(b) respectively, while $n_{0,1D}$ accounts for an offset due to intensity fluctuations between the images. The phase φ would be read out for an interferometric measurement of e.g. inertial forces. In this study however, we have restricted ourselves to the contrast information since the phase stability over multiple drops could not yet be guaranteed for the times presented.

For long observation times a tilt of the interference fringes with respect to the z-axis is observed, which is compensated by aligning the image before we calculate the column density along z. Error bars in Fig.3 are standard deviations calculated via the fitted model and multiple noise realizations.

Figure S1 displays the decaying signal to noise ratio

$$
SNR \equiv \frac{n_{max,1D}}{\nu_{rms}} \quad (4)
$$

of the integrated atomic density with and without delta kick cooling (DKC) as a function of time, with ν_{rms} being the RMS of the fit residuals. Due to the spreading of the atomic wave packet, in the linear regime the 1D atomic density decreases according to

$$
n_{max,1D} = \frac{N}{\sqrt{8\pi}\sigma_y} \approx \frac{N}{\sqrt{8\pi}\,(\alpha T_{ex} + \beta)} \quad (5)
$$

with the total atom number N, expansion rate α and an offset β. Thus, in the case of DKC the SNR falls off with a slower rate and is doubled by overlapping the output ports, allowing us to detect the atoms after longer times T_{ex} than in the free case.

For longer interferometer times $2T - \delta T$ the fit routine does not converge to the expected fringe period, which is kept as a free parameter in the data evaluation. These data (open red squares and open black triangles in Fig. S1) were not included in Fig. 3. Fitting the discarded data with the fringe period predicted by Eq. (8) yields a finite contrast. These values were confronted with the contrast obtained by applying the same fit routine to synthetic test signals, which were generated from Eq. 3 for a vanishing contrast ($C = 0$) with multiple noise realizations in compliance with the observed SNR. As depicted in the inset of Fig. S1, the contrast resulting from the analysis of the test data (dashed line) was indeed equal or higher than the one obtained for the discarded experimental data, thus confirming the loss of contrast. The dashed curve indicates that the minimum detectable contrast is limited by the SNR.
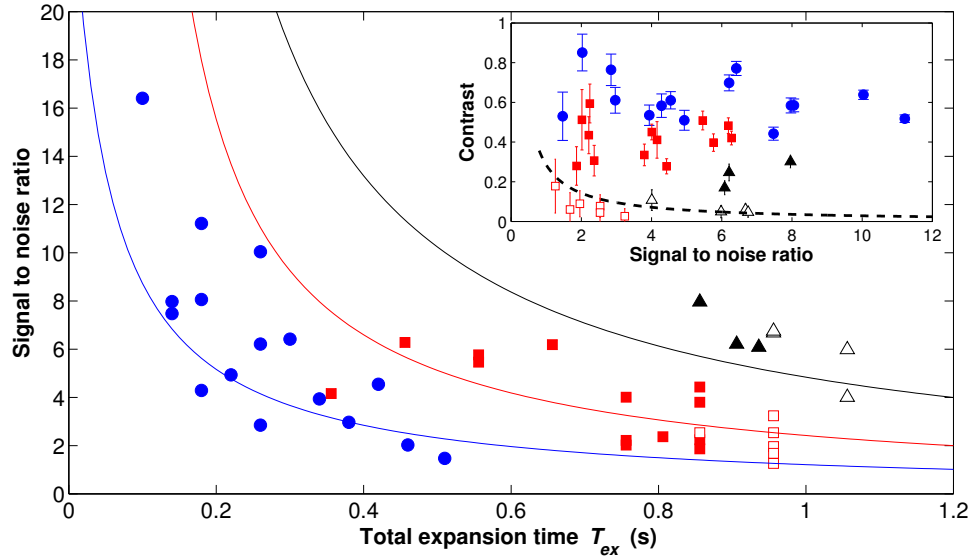
5

Figure S1: Signal to noise ratio (SNR) of the integrated atomic density forming the interference patterns as a function of the total expansion time T_{ex} with (red squares) and without (blue dots) delta kick cooling (DKC) as well as for overlapping interferometer ports (black triangles). With DKC the SNR decreases with a slower rate than without and is further increased when both interferometer ports are detected before they are fully separated spatially. The scatter is caused by atom number fluctuations and by the detection intensity varying between individual drops due to the atoms being located in another position within the Gaussian profile of the laser beam. To facilitate the comparison of the three cases, the curves (blue, red, black) show the decay according to Eq.(4) and (5) using the measured expansion rates, mean atom number and noise. Towards longer expansion times (open black triangles and red squares), the period of the fringe pattern could not be obtained by fitting the data with the period as a free parameter, so these data points were discarded in Fig. 3. The inset presents the observed contrast in relation to the SNR for all datapoints. The contrast was obtained by fitting the function n_{1D} given by. Eq. (3) to the experimental data (blue circles, red squares and black triangles) and to synthetic data (black dashed line) generated from Eq. (3) for a vanishing contrast ($C = 0$) and noise in compliance with the observed SNR. For the synthetic data as well as for the discarded experimental data points the contrast was derived from fits with the fringe period fixed to the theoretical value. The agreement of both confirms the loss of contrast for long interferometer times $2T - \delta T$. For smaller SNRs, the minimum detectable contrast increases, as indicated by the dashed line.

6

Asymmetric Mach-Zehnder interferometer

We now turn to the theoretical description of our asymmetric Mach-Zehnder interferometer (AMZI). Here we only outline the essential ingredients of our formalism and present the main results relevant for the experiments described in our article. A more detailed treatment will be subject of a future publication.

Building blocks

We describe the BEC in our trap by a time- and position-dependent macroscopic wave function $\psi = \psi(\boldsymbol{r}, t)$ determined by the non-linear Gross-Pitaevskii equation (GPE). In all experiments reported in our article the trap is well approximated by a parabolic potential V which is also time-dependent since the BEC is released by turning off the trap. Another reason for considering a time-dependent V emerges from the need to describe the technique of delta-kick cooling in our experiments. In these cases, the GPE can be well approximated by an almost analytical solution $\psi = e^{i\Phi} \psi^{(\mathrm{TF})}(\boldsymbol{r}, t)$ consisting of the product of a phase factor and the Thomas-Fermi (TF) ground state wave function of the trap with a time-dependent rescaling of the spatial coordinates[15, 37-39]. The so-defined time-dependent wave function $\psi^{(\mathrm{TF})}(\boldsymbol{r}, t)$ is real and normalized at all times. Moreover, the phase Φ of ψ does not only depend on the space-time variables $\boldsymbol{r}$ and t but also on the center-of-mass (COM) motion of the BEC expressed by the time-dependent coordinate $\boldsymbol{\mathcal{R}} = \boldsymbol{\mathcal{R}}(t)$ and momentum $\boldsymbol{\mathcal{P}} = \boldsymbol{\mathcal{P}}(t)$. In contrast, the TF-wave function $\psi^{(\mathrm{TF})}$ is only a function of the difference $\boldsymbol{r} - \boldsymbol{\mathcal{R}}(t)$ and t.

The interaction of the BEC with a Bragg pulse at a time t_{p} can change the instantaneous momentum $\boldsymbol{\mathcal{P}}(t_{\mathrm{p}})$ of the COM motion by $\pm \hbar \boldsymbol{k}$, where $\boldsymbol{k}$ is the effective wave vector of the Bragg pulse, but leaves the position $\boldsymbol{\mathcal{R}}(t_{\mathrm{p}})$ untouched. Moreover, the wave imprints a phase on the BEC given by the sum of $\boldsymbol{k} \cdot \boldsymbol{\mathcal{R}}(t_{\mathrm{p}})$ and the phase $\phi(t_{\mathrm{p}})$ of the Bragg pulse. The wave function altered in this way is also multiplied by the imaginary factor $(-i)$ resulting from the

time-dependent Schrödinger equation.

When the parameters of the Bragg pulse are chosen to act as a 50:50 beam splitter, the BEC partly experiences a recoil and partly continues undisturbed with equal amplitudes. As a result, the COM motion is in a superposition of the original momentum $\mathcal{P}$ and $\mathcal{P} + \hbar\boldsymbol{k}$, or $\mathcal{P}$ and $\mathcal{P} - \hbar\boldsymbol{k}$ with equal weights $1/\sqrt{2}$. When the pulse acts as a mirror, it changes the momentum by $+\hbar\boldsymbol{k}$ or $-\hbar\boldsymbol{k}$ with unit probability.

Wave functions at the exit ports

The description of the BEC with the help of the GPE and the effect of the Bragg pulses outlined above constitute the main building blocks of our formalism to analyze the AMZI shown in Fig. S2. Our goal is to obtain the wave functions Ψ_I and Ψ_II of the BEC at the two exit ports I and II of the interferometer, which differ by the COM momentum of the BEC.
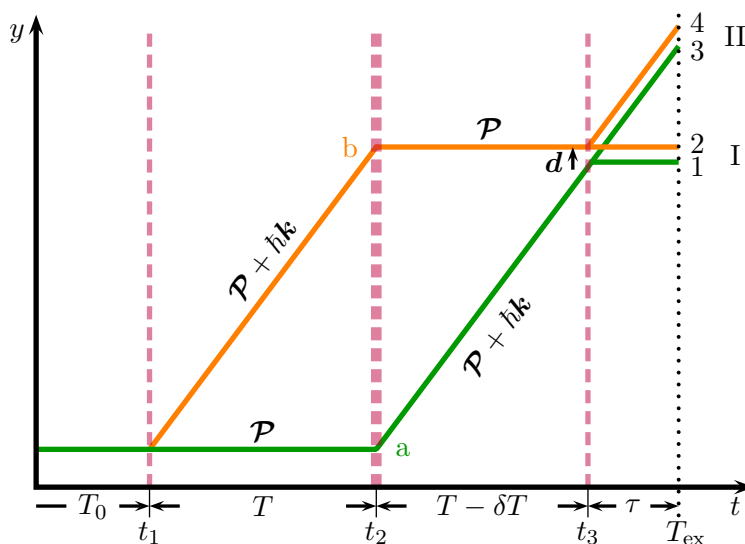

Figure S2: Diagram of the COM trajectories for our AMZI with labels for the two branches (a and b), the two exit ports (I and II) and the equal-momentum trajectories at each exit port ($\{1, 2\}$ and $\{3, 4\}$). The horizontal axis corresponds to time and the vertical one to position along the y-direction. The dashed lines depict the Bragg laser pulses whereas the dotted line represents the detection pulse for absorption imaging.

8

Indeed, in port I it is the initial momentum $\mathcal{P}$ since both paths 1 and 2 have experienced two opposite momentum kicks. However, in port II it is $\mathcal{P} + \hbar\boldsymbol{k}$ since both paths have received an odd number of kicks which is different in paths 3 and 4. In path 4 we have three exchanges of momenta, that is $\hbar\boldsymbol{k} - \hbar\boldsymbol{k} + \hbar\boldsymbol{k} = \hbar\boldsymbol{k}$, whereas in path 3 we have only a single one, that is $+\hbar\boldsymbol{k}$.

In order to find the wave functions Ψ_I and Ψ_II at the two exit ports, we now solve the GPE including the momentum kicks imparted by the Bragg pulses starting with the initial TF-wave function of the ground state of the trap. We switch off the trap at $t = 0$ and evolve the BEC according to the GPE. This dynamics gives rise to a phase factor Φ_0 and a spreading of the TF-wave function. The Bragg pulse at $t_1 \equiv T_0$ serving as a beam splitter either changes the COM motion due to the momentum transfer $\hbar\boldsymbol{k}$ and imprints phases on the BEC in addition to the Φ_0 accumulated before the pulses, or leaves it untouched. After the pulse the two BECs evolve for the time T according to the GPE in the absence of a potential, which provides us with additional dynamical phases.

The second Bragg pulse at $t_2 \equiv T_0 + T$ acts as a mirror and imprints again a phase but also transfers momentum with unit probability. Hence, no splitting of the trajectories occurs. The ensuing dynamics of the BECs according to the GPE adds new dynamical phases, and the two BECs on the paths a and b approach each other till at $t_3 \equiv T_0 + 2T - \delta T$ the third Bragg pulse implementing another beam splitter mixes them. Again the phases of the pulse and the instantaneous positions of the BEC are mapped onto the wave functions.

At this moment it becomes important that our interferometer is asymmetric since the time T between the first and the second Bragg pulse is different from the one between the second and the third by an amount δT, as indicated in Fig. S2. As a consequence, at each exit port the interfering BECs are slightly shifted with respect to each other by an amount $\boldsymbol{d} \equiv (\hbar\boldsymbol{k}/m)\delta T$ where m is the mass of the atom.

When this displacement $\boldsymbol{d}$ is small compared to the extension of the BEC, we can neglect it in the arguments of $\psi^{(\text{TF})}$, which acts as envelope of the wave functions contributing to each exit port. However, it is of crucial importance for the phases accumulated by the BEC on the two paths through the interferometer, since they depend in a sensitive way on the COM motion.

An execution of this procedure yields for $t_3 < t$ the expressions

$$\Psi_{\text{I}} \cong \frac{1}{2}\, \text{e}^{i\alpha_{\text{I}}}\, \psi^{(\text{TF})}\left(\boldsymbol{r} - \boldsymbol{\mathcal{R}}_1(t); t\right)\left\{1 + \exp\left[i\left(\alpha + \frac{m\boldsymbol{d}}{\hbar t}\left(\boldsymbol{r} - \boldsymbol{\mathcal{R}}_1(t)\right)\right)\right]\right\} \tag{6}$$

and

$$\Psi_{\text{II}} \cong \frac{1}{2}\, \text{e}^{i\alpha_{\text{II}}}\, \psi^{(\text{TF})}\left(\boldsymbol{r} - \boldsymbol{\mathcal{R}}_3(t); t\right)\left\{1 - \exp\left[i\left(\alpha + \frac{m\boldsymbol{d}}{\hbar t}\left(\boldsymbol{r} - \boldsymbol{\mathcal{R}}_3(t)\right)\right)\right]\right\} \tag{7}$$

for the wave functions Ψ_{I} and Ψ_{II} in the two exit ports. Here α_{I}, α_{II} and α contain the phases imprinted by the Bragg pulses as well as the dynamical phases accumulated by the BEC along the two paths and determined by the GPE.

The two wave functions are centered around the positions $\boldsymbol{\mathcal{R}}_1(t)$ and $\boldsymbol{\mathcal{R}}_3(t)$ of the COM trajectory at t and the spatially dependent phase, leads to oscillations with wavelength

$$l \equiv \frac{2\pi\hbar t}{m|\boldsymbol{d}|}\ . \tag{8}$$

BEC densities: Near-field versus far-field

From Fig. S2 we note that at the final beam splitter, that is at t_3, we have the equality $\boldsymbol{\mathcal{R}}_1(t_3) = \boldsymbol{\mathcal{R}}_3(t_3)$, and due to the momentum difference of $\hbar\boldsymbol{k}$ between $\boldsymbol{\mathcal{R}}_3$ and $\boldsymbol{\mathcal{R}}_1$ we find the relation

$$\boldsymbol{\mathcal{R}}_3(t_3 + \tau) = \boldsymbol{\mathcal{R}}_1(t_3) + \frac{\hbar\boldsymbol{k}}{m}\tau \tag{9}$$

for later times.

When $(\hbar|\boldsymbol{k}|/m)\tau$ is larger than the extension of the BEC given by $\psi^{(\text{TF})}$, we can separate the two exits and the BEC densities W_{I} and W_{II} following from (6) and (7) read

$$W_{\text{I}} = \left(\psi^{(\text{TF})}\left(\boldsymbol{r} - \boldsymbol{\mathcal{R}}_1(t); t\right)\right)^2 \cos^2\left[\frac{\alpha}{2} + \frac{m\boldsymbol{d}}{2\hbar t}\cdot\left(\boldsymbol{r} - \boldsymbol{\mathcal{R}}_1(t)\right)\right] \tag{10}$$

10

and

$$W_{\mathrm{II}} = \left(\psi^{(\mathrm{TF})}\left(\boldsymbol{r} - \boldsymbol{\mathcal{R}}_3(t); t\right)\right)^2 \sin^2\left[\frac{\alpha}{2} + \frac{m\boldsymbol{d}}{2\hbar t}\left(\boldsymbol{r} - \boldsymbol{\mathcal{R}}_3(t)\right)\right] . \tag{11}$$

Three features stand out most clearly in these expressions valid in the far-field limit: (i) The envelopes of W_{I} and W_{II} are given by the time-dependent TF-profiles $\left(\psi^{(\mathrm{TF})}\right)^2$ centered at the COM coordinates $\boldsymbol{\mathcal{R}}_1(t)$ and $\boldsymbol{\mathcal{R}}_3(t)$ of the BEC at t. (ii) The arguments of the trigonometric functions in W_{I} and W_{II}, which are also measured with respect to $\boldsymbol{\mathcal{R}}_1(t)$ and $\boldsymbol{\mathcal{R}}_3(t)$, have identical wavelengths given by (8) and depend on the total time from the release of the BEC from the trap till the measurement, denoted by T_{ex} in the paper, and (iii) the two distributions are complementary, that is W_{I} follows a cosine- and W_{II} a sine-function.

It is also interesting to note that we would have obtained the same expression for W_{I} if we had considered the free propagation of a superposition of two identical wave packets initially separated by $\boldsymbol{d}$ and with momentum $\boldsymbol{\mathcal{P}}$. Indeed, the fringe spacing l in both situations is identical. In the corresponding analogy giving rise to W_{II} the wave packets have the momentum $\boldsymbol{\mathcal{P}} + \hbar\boldsymbol{k}$. It is in this sense that the AMZI is analogous to Young's double-slit configuration.

In the opposite limit, when $(\hbar|\boldsymbol{k}|/m)\tau$ is smaller than the extension of the BEC, the two wave functions Ψ_{I} and Ψ_{II} create an interference term $I \equiv \Psi_{\mathrm{I}}^*\Psi_{\mathrm{II}} + $ c.c. in the probability

$$W = |\Psi_{\mathrm{I}} + \Psi_{\mathrm{II}}|^2 = W_{\mathrm{I}} + W_{\mathrm{II}} + I . \tag{12}$$

From (6) and (7) we note that I contains the phase difference $\alpha_{\mathrm{I}} - \alpha_{\mathrm{II}}$, which apart from many other phases involves a term $\boldsymbol{k} \cdot \boldsymbol{r}$ due to the different COM momenta of the paths 3 and 1 after the last beam splitter and gives rise to oscillations of the term I with the optical wavelength. Our detectors cannot resolve such small structures and average instead over them, so that the contributions of the interference term I vanishes.

When we now arrange the detection time τ such that

$$\frac{\boldsymbol{d} \cdot \boldsymbol{k}\tau}{2t} = \frac{\pi}{2} , \tag{13}$$

11

we can make a cosine- out of the sine-function in W_{II}, which amounts to a shift by $l/2$ so that the maxima of W_{I} and W_{II} coincide.

Moreover, we recall that we are in the near-field regime where we cannot distinguish the two exit ports, that is we can replace the COM coordinate $\boldsymbol{\mathcal{R}}_3$ by $\boldsymbol{\mathcal{R}}_1$ in the prefactor $\psi^{\text{(TF)}}$ of W_{II}, which finally yields the expression

$$W = 2\left(\psi^{\text{(TF)}}\left(\boldsymbol{r} - \boldsymbol{\mathcal{R}}_1(t);t\right)\right)^2 \cos^2\left[\frac{\alpha}{2} + \frac{m\boldsymbol{d}}{2\hbar t}\left(\boldsymbol{r} - \boldsymbol{\mathcal{R}}_1(t)\right)\right] \tag{14}$$

for the BEC density.

Hence, by working in the near field region, we have obtained a factor of two in the intensity of W which allowed us to obtain a higher signal and extend our measurements to longer times. In Fig. 3 such measurements are indicated by triangles.

We conclude by noting that in the experimental realization reported in our article the laser phases were not stabilized. Therefore, the phase α in eqs. (10), (11) and (14), and consequently the location of the fringes, fluctuated from shot to shot.